Journal of Catalysis 312 (2014) 17–25

Contents lists available at ScienceDirect

Journal of Catalysis

journal homepage: www.elsevier.com/locate/jcat

CO oxidation on PtSn nanoparticle catalysts occurs at the interface of Pt and Sn oxide domains formed under reaction conditions

William D. Michalak [a,b,*], James M. Krier [a,b], Selim Alayoglu [a,b], Jae-Yoon Shin [c], Kwangjin An [b], Kyriakos Komvopoulos [d], Zhi Liu [e], Gabor A. Somorjai [a,b,*]

[a] Chemical Science and Material Science Divisions, Lawrence Berkeley National Laboratory, Berkeley, CA 94720, United States
[b] Department of Chemistry, University of California, Berkeley, CA 94720, United States
[c] Department of Chemical Engineering, University of California, Berkeley, CA 94720, United States
[d] Department of Mechanical Engineering, University of California, Berkeley, CA 94720, United States
[e] Advanced Light Source, Lawrence Berkeley National Laboratory, Berkeley, CA 94720, United States

ARTICLE INFO

Article history:
Received 25 November 2013
Accepted 8 January 2014
Available online 12 February 2014

Keywords:
Pt
Sn
Nanoparticle
Catalysis
Carbon monoxide oxidation
Interface
Ambient pressure X-ray photoelectron spectroscopy
Redox couple

ABSTRACT

The barrier to CO oxidation on Pt catalysts is the strongly bound adsorbed CO, which inhibits O_2 adsorption and hinders CO_2 formation. Using reaction studies and *in situ* X-ray spectroscopy with colloidally prepared, monodisperse ~2 nm Pt and PtSn nanoparticle catalysts, we show that the addition of Sn to Pt provides distinctly different reaction sites and a more efficient reaction mechanism for CO oxidation compared to pure Pt catalysts. To probe the influence of Sn, we intentionally poisoned the Pt component of the nanoparticle catalysts using a CO-rich atmosphere. With a reaction environment comprised of 100 Torr CO and 40 Torr O_2 and a temperature range between 200 and 300 °C, Pt and PtSn catalysts exhibited activation barriers for CO_2 formation of 133 kJ/mol and 35 kJ/mol, respectively. While pure Sn is readily oxidized and is not active for CO oxidation, the addition of Sn to Pt provides an active site for O_2 adsorption that is important when Pt is covered with CO. Sn oxide was identified as the active Sn species under reaction conditions by *in situ* ambient pressure X-ray photoelectron spectroscopy measurements. While chemical signatures of Pt and Sn indicated intermixed metallic components under reducing conditions, Pt and Sn were found to reversibly separate into isolated domains of Pt and oxidic Sn on the nanoparticle surface under reaction conditions of 100 mTorr CO and 40 mTorr O_2 between temperatures of 200–275 °C. Under these conditions, PtSn catalysts exhibited apparent reaction orders in O_2 for CO_2 production that were 0.5 and lower with increasing partial pressures. These reaction orders contrast the first-order dependence in O_2 known for pure Pt. The differences in activation barriers, non-first-order dependence in O_2, and the presence of a partially oxidized Sn indicate that the enhanced activity is due to a reaction mechanism that occurs at a Pt/Sn oxide interface present at the nanoparticle surface.

1. Introduction

CO poisons Pt surfaces and prevents the formation of CO_2 by inhibiting O_2 adsorption. While pure Sn becomes readily oxidized in the presence of O_2 and does not react with CO, the rate of CO oxidation can be improved by incorporating Sn into Pt catalysts [1–6]. The barrier to understanding the mechanism of CO oxidation on PtSn, and even pure Pt catalysts, is knowledge of the structure and chemical environment of the surface and the nature of the catalytic active phase. The key in determining the true active phase of the catalyst is monitoring the atomic- and molecular-level details of surface atoms and reactants on the surface of the catalyst as the reaction proceeds. Nanoparticle catalysts can undergo significant structural and compositional changes that depend on the temperature and gas atmosphere during pre-treatment, reaction, and post-treatment [7–9]. Often, prenatal and postmortem spectroscopic characterization studies are used to understand the nature of the catalytic active phase. This approach often leads to diverse conclusions because the catalyst surface changes with different treatments and when samples are transferred from reactor to characterization tool. In order to make definitive conclusions about the catalyst's active phase using spectroscopic tools, the catalyst must be studied under reaction conditions.

Catalysts that are used industrially and commonly for laboratory kinetic reaction studies present challenges for atomic-level spectroscopic investigations because the porous supports

* Corresponding authors at: Chemical Science and Material Science Divisions, Lawrence Berkeley National Laboratory, Berkeley, CA 94720, United States. Fax: +1 510 643 9668.
E-mail addresses: wmichalak@gmail.com (W.D. Michalak), somorjai@berkeley.edu (G.A. Somorjai).

http://dx.doi.org/10.1016/j.jcat.2014.01.005
0021-9517/

attenuate signal and the active catalyst is polydisperse in size and composition. In order to observe changes in catalyst surfaces under reaction conditions, nanoparticle catalysts should not be embedded deep within pores of the support material. An effective method that allows for both reaction studies and spectroscopic observation under reaction conditions is deposition of colloidally prepared nanoparticles onto two-dimensional supports such as Si wafers [10,11]. Understanding how structure and composition of catalysts correlate with catalytic activity and selectivity requires ensembles of nanoparticles that have monodisperse size, shape, and composition distributions. Achieving monodispersity in size and composition is challenging when creating nanoparticles with incipient impregnation methods used in industry (i.e., reducing the metal precursors directly onto a mesoporous or microporous supports such as silica or alumina) due to uncontrolled mixing of the precursors at the liquid–solid interface, or from sequential reduction of multiple elements. However, an alternative synthesis approach that provides control over nanoparticle size and composition is inorganic colloidal synthesis [12,13].

In this work, we use ambient pressure X-ray photoelectron spectroscopy (APXPS) [14,15] to monitor the chemical composition and electronic environment of well-defined, colloidally prepared PtSn nanoparticle catalysts under various gas atmospheres. PtSn catalysts exhibit dynamic segregation with an intermixed Pt–Sn phase under reducing conditions and separated metallic Pt and oxidic Sn domains under CO oxidation reaction atmospheres. By intentionally poisoning the Pt surface sites with CO, we show that the enhanced activity displayed by PtSn catalysts is due to the presence of Sn, which allows for O_2 adsorption and dissociation and a Pt/Sn oxide interface where SnO is reduced by CO. An alternative and more facile reaction mechanism at the interface is confirmed by measurements of the effective activation barriers and reaction rate dependencies with respect to O_2 and CO.

2. Experimental methods and materials

2.1. Materials

Hexachloroplatinic acid ($H_2PtCl_6{\cdot}6H_2O$, 99%), tin chloride ($SnCl_2$, 98%), tin(II) acetate ($Sn(C_2H_3O_2)_2$, 99%), poly(vinylpyrrolidone) (PVP, MW = 29,000/55,000 amu), ethylene glycol (reagent grade), hydrochloric acid (HCl, 2 M), sodium hydroxide (NaOH, 99.9%), sodium borohydride ($NaBH_4$, 99.9%), acetone (99%), tetraorthosilicate (99.9%), and ammonium hydroxide (99.9%) were manufactured by Sigma Aldrich. 1,5-pentanediol (95%), ethanol (100%), and hexane (99.9%) were manufactured by Fluka, KOPTEC, and BDH, respectively. Oxygen (5.0 UHP), carbon monoxide (5.0 UHP), and helium were purchased from Praxair. Polished Si(100) wafers were purchased from Addison Engineering. To minimize Fe or Ni carbonyls in the reactant gases, CO was stored in an Al cylinder and was passed through Cu tubing heated to 300 °C immediately before the reactor inlet.

2.2. Nanoparticle synthesis

Pt, PtSn, and Sn nanoparticles were prepared using inorganic colloidal methods as described previously with a PVP capping ligand [10,16,17]. The syntheses can be conducted using different initial amounts of precursors as long as the relative ratios remain constant. Polyhedral platinum nanoparticles of 2 nm average diameter were prepared by mixing 10 mL of ethylene glycol, 100 mg of $H_2PtCl_6{\cdot}6H_2O$ (1.9×10^{-4} mol), and 5 mL of a 0.5 M NaOH solution (0.1 g) in a 25-mL three-neck round-bottom flask. The flask was sealed with septa, and the residual air atmosphere was evacuated by three cycles of vacuum pumping followed by an Ar purge. The synthesis was conducted at 160 °C with vigorous stirring in Ar flow for 2 h. After the colloid returned to room temperature, 20.3 mg of PVP (0.18 mol) was added followed by vigorous stirring for 20 min. Finally, 100 mL of acetone was added to the solution, and the particles were precipitated by centrifugation at 4000 rpm (VWR Clinical 50) for ~10 min. Further washing with ethanol and hexane was performed three times to remove residual molecular fragments from the particle surface. These nanoparticles, as well as the PtSn and Sn nanoparticles, were stored in ethanol under refrigeration before their use in kinetic and spectroscopic studies.

Polyhedral PtSn nanoparticles of 2.2 nm average diameter were prepared by mixing 10 mL of ethylene glycol, 28 mg of $H_2PtCl_6{\cdot}6H_2O$ (7×10^{-5} mol), 13 mg of $SnCl_2$ (7×10^{-5} mol), and 111 mg of PVP (1×10^{-3} mol) in a 25-mL three-neck round-bottom flask. The synthesis was conducted at 160 °C with vigorous stirring in Ar flow for 2 h. After the colloid returned to room temperature, 40 mL of acetone was added to the solution and the particles were precipitated by centrifugation and washed with the same procedure used for the Pt nanoparticles.

To synthesize polyhedral Sn nanoparticles of 6 nm average diameter, 0.14 g of $Sn(OAc)_2$ (6×10^{-4} mol) and 1.7 g of PVP (1.5×10^{-2} mol) were loaded into a 100-mL three-neck round-bottom flask in a glove box. After adding 20 mL of dried 1,5-pentanediol into the precursor solution, the flask was evacuated by vacuum pumping followed by an Ar purge and heating to 100 °C with vigorous stirring. A reducing agent, which was prepared by dissolving 0.23 g of $NaBH_4$ in 60 mL of dried 1,5-pentanediol, was quickly injected into the precursor solution, and the reaction was maintained at 100 °C for 15 min. After cooling to room temperature, acetone was added to the solution and the nanoparticle solids were precipitated by centrifugation and washed with the same procedure used for the Pt nanoparticles.

2.3. Preparation of silica encapsulated Pt and PtSn nanoparticles for reaction studies

For the reaction studies, the Pt and PtSn nanoparticle catalysts were encapsulated in a porous silica shell to eliminate sintering during the long-term high-temperature experiments [18]. The nanoparticles were encapsulated in a SiO_2 shell using a modified sonication-assisted Stöber method with PVP as a pore structuring agent [19,20]. To prepare the shell surrounding the nanoparticles, a 50 μL aliquot of the as-prepared colloid was mixed by sonication (Branson, 3510) with 15 mL of ethanol in a 20 mL scintillation vial. While the mixture remained in the sonication bath, 2 ± 1 μL of TEOS was added (the total amount varied depending on the concentration of the nanoparticle solution). Following ~30 s of continued sonication, 2.25 mL of NH_3OH was added drop-wise over a period of 5 min. The solution was left in the sonication bath for 2 h. The ~21 mL solution of core–shell nanoparticles was washed with 21 mL of a 50:50 mixture of acetone and hexane and was precipitated by centrifugation for 10 min.

2.4. Catalyst sample preparation (Langmuir–Blodgett film deposition)

For kinetic and spectroscopic studies, nanoparticles were supported on two-dimensional surfaces. The use of a two-dimensional support differs from common catalytic studies that use high surface area materials (e.g., silica, alumina, or carbon) as catalyst supports. Surface-sensitive X-ray spectroscopy only probes the particles at the exterior of the high surface area three-dimensional supports. For kinetic studies, SiO_2-encapsulated Pt or PtSn nanoparticles were deposited onto a Si(100) wafer using a Langmuir–Blodgett trough (Kibron, MTX). For spectroscopic studies, the Pt or PtSn nanoparticles were supported on Au-coated Si wafers. Both supports exhibited negligible activity for CO oxidation.

Before the Langmuir–Blodgett deposition, the Si surfaces were exposed to strong oxidizers (e.g., piranha or Nochromix) to remove organic residues and make them hydrophilic (oxidizers hydroxylate the silica). Nanoparticles were dispersed in a 50:50 chloroform:ethanol mixture and deposited onto an ultrapure water subphase (18.2 MΩ cm). Following the evaporation of the solvent and equilibration of particles (30–60 min), the two-dimensional layer of particles was compressed at a rate of 5 mm/min to create a close-packed monolayer. When the monolayer of particles was compressed to a surface pressure in the range of 30–35 mN/m, the substrates were withdrawn at a rate of 2 mm/min while maintaining a constant pressure. Surface tension was monitored using Wilhelmy probe made of a PtIr wire.

Following deposition, the core–shell nanoparticles supported on the wafers were calcined in a tube furnace (Lindberg Blue M) at 350 °C in ambient conditions to remove the PVP capping agent and create pores in the silica shell [18]. The samples were stored in ambient atmosphere before use.

2.5. Morphological characterization

Nanoparticle morphology and size were examined using a transmission electron microscope (TEM, JEOL 2100) operated at 200 kV. The nanoparticle size was measured using ImageJ v. 1.45s software (NIH). Particle size distributions were obtained with >300 particles. Nanoparticles were reclaimed from the silica wafers after heat treatments and reactions by rinsing the Si wafer surface in ethanol and collecting the rinsing agent. The dissolved nanoparticles were then precipitated by centrifugation, redispersed in ethanol, and dropcast onto TEM grids for imaging.

Pt and PtSn catalysts had an average diameter of 2.1 ± 0.4 and 2.2 ± 0.4 nm, respectively. For the CO oxidation reaction studies, the catalysts were encapsulated within inorganic porous silica shells to provide sintering resistance during long-term high-temperature studies. We did not encapsulate the catalysts for the spectroscopic studies, which were performed over relatively shorter periods of time. The encapsulation is important to maintain catalyst morphology when catalysts are supported on two-dimensional, flat, supports such as Si (or silica) wafers. The nature of the smooth support coupled with the size-dependent melting point depression of nanometer size metals [21,22] increases the rate of agglomeration. However, catalysts that are coated with porous silica shells have thermal stability up to 700 °C [18]. We were able to obtain porous shells that encapsulate multiple nanoparticles as shown in the Supplementary information Fig. S1. The encapsulated nanoparticles demonstrate the particle morphology and size (monodispersity of the nanoparticles is displayed by nanoparticle size distributions shown in the insets). Negligible changes in nanoparticle morphology were observed after multiple treatment/reaction cycles at temperatures up to 350 °C. PtSn catalysts that were reclaimed after many cycles of treatment and reaction cycles are shown in Fig. S1. The average particle size of a sample of PtSn cores after performing reaction studies was 2.3 ± 0.5 nm.

2.6. Chemical characterization

Chemical characterization of the catalysts was performed using lab-based and synchrotron-based XPS systems and energy dispersive spectroscopy (EDS). Lab-based PHI 5400 XPS system was used under ultra-high vacuum conditions with an Al anode operated at 350 W. Samples were maintained at room temperature and 5×10^{-9} Torr vacuum during characterization. The synchrotron-based APXPS system at beamline 9.3.2 at the Advanced Light Source was operated under ultrahigh vacuum (1×10^{-9} Torr), 100 mTorr H_2 reducing conditions, and a reaction gas mixture of 100 mTorr CO and 40 mTorr O_2. The sample was heated to temperatures between 100 and 375 °C using a resistive heating element positioned in contact with the sample [23]. To maintain similar penetration depths for Pt and Sn, we kept the kinetic energy constant for the Sn and Pt signals using photon energies of 320 and 740 eV, respectively (unless otherwise noted).

Curve fitting of the Sn $3d_{5/2}$, Pt 4f, and O 1s XPS spectra was performed using CasaXPS v.2.3.15 software. The binding energies in the spectra were calibrated using the Au $4f_{7/2}$ feature at a binding energy of 84 eV [24]. The intensity of the Sn $3d_{5/2}$, Pt 4f, and O 1s spectra was normalized by the Au $4f_{7/2}$ peak intensity at the constant photon energy to account for signal attenuation due to X-ray absorption by ambient gases. During fitting, the position and full width at half maximum (FWHM) of the Sn $3d_{5/2}$, Pt 4f and O 1s features were held constant across different gas environments with a unique FWHM value for each chemical state (c.f. Table 1); only the area was unconstrained. The Pt 4f orbitals were described by two features for each hybrid state. We used a constant spin–orbit splitting value of 3.3 eV and a branching ratio of 0.75 for 5/2:7/2 states. The Sn $3d_{5/2}$ spectral features were fit using an asymmetric Lorentzian distribution (LA(1.1, 1.7, 35)), and the Pt 4f and O 1s spectral features were fit using a sum of Gaussian and Lorentzian distributions (SGL(35)) as performed by Jugnet et al. [4]. The spectra were fit using a Shirley background. Relative sensitivity factors of 5.575, 4.725, and 0.71 were used for the Pt 4f, Sn $3d_{5/2}$, and O 1s spectra [25].

EDS measurements of ensembles of atoms were performed with an electron source operated at 120 kV on a Cu TEM grid (EDAX Si(Li) detector, Ametek, Inc).

2.7. Kinetic measurements

CO oxidation studies were performed in a 1-L stainless steel chamber that was sealed with Conflat flanges and Cu or Viton gaskets. A mechanical rotary pump was used to remove ambient gases before introducing the reactant gases. The pressure of the reactant gases was monitored with a capacitance manometer pressure gauge (MKS Baratron). A metal bellows recirculating pump (Senior Aerospace MB-21) was used to mix the gases within the chamber to eliminate mass transfer issues. A pervasive problem encountered with studies of CO oxidation is the local exotherms caused by the −284 kJ/mol thermodynamic energy difference between CO and CO_2. The effects of temperature drift were minimized using a water-cooled heating manifold in conjunction with the resistively heated boronitride plate (Momentive) to support and heat the catalyst sample. In addition, gas-phase dilution of the reactant gases with He provided efficient conductive heat transfer away from the sample. The temperature of the sample was monitored using a type-K thermocouple. The conversion of CO to CO_2 was monitored using a differentially pumped quadrupole mass spectrometer (QMS, Stanford Research Systems, RGA 200) with a turbomolecular

Table 1
Peak assignments and full width half maximum for Sn $3d_{5/2}$, Pt 4f, and O 1s X-ray photoelectron spectroscopy features.

Sn $3d_{5/2}$	Location (eV)	FWHM	Pt 4f	Location (eV)	FWHM	O 1s	Location	FWHM
Sn^0	485.2	0.8	Pt^0	70.8–71.1	0.9	SnO_x	530.4	1.4
Sn(Pt)	485.7	0.9	Pt(Sn)	71.4	0.9			
Sn^{2+}	486.4	0.9	Pt–CO/O	72.5	1.6			
Sn^{4+}	487.3	1.3						

pump to maintain vacuum pressures (Pfeiffer, TMU-260). The reaction chamber was connected to the QMS via a 10 μm ID by 1 m length silica capillary (Restek), which yielded a pressure of 2×10^{-6} Torr in the QMS chamber with 760 Torr gas pressure in the reactor. Activity measurements were performed under differential conditions, in which conversion was <10%.

Measurements of reaction orders for O_2 were measured in the APXPS system at beamline 9.3.2 at the Advanced Light Source.

3. Results

3.1. CO oxidation reaction studies with Pt and PtSn nanoparticle catalysts

The kinetic behaviors for CO oxidation on Pt and PtSn nanoparticle catalysts were studied by measuring the net effective activation barrier (ΔE_{eff}) and O_2 reaction orders. In the presence of gaseous CO at temperatures <300 °C, Pt surfaces (and modified Pt surfaces) are highly populated by chemisorbed CO. High CO occupancy inhibits dissociative adsorption of O_2 at Pt sites [6,26–28]. To determine the effects of Sn in the PtSn catalyst over ΔE_{eff}, we chose to intentionally poison the Pt active sites using CO-rich reaction conditions (100 Torr CO and 40 Torr O_2). Previous measurements of CO oxidation rates on Pt under vacuum and ambient pressures indicate negligible pressure gap [29]. Reaction orders in O_2 were measured at mTorr pressures with the simultaneous XPS measurements and at Torr range pressures, which were the conditions used to measure ΔE_{eff}. With a high population of CO adsorbed on the surface, we correlate any changes observed in the reaction mechanisms (determined from ΔE_{eff} and O_2 reaction orders) to the presence of Sn alone.

3.2. Effective activation barriers for CO oxidation

To compare the CO oxidation activity on the Pt and PtSn catalysts, we use measurements of ΔE_{eff} rather than turnover frequencies (TOF). We do not provide TOF values because we have not identified an appropriate method to count active sites on the PtSn catalysts, which we show to be different than on pure Pt catalysts. To determine ΔE_{eff} values on Pt and PtSn catalysts, the rates of CO_2 formation (r) were measured as a function of temperature in the range of 200–300 °C and a gas mixture of 100 Torr CO, 40 Torr O_2, and 630 Torr He. Arrhenius plots ($\ln(r)$ versus T^{-1}) for the Pt (red) and PtSn (blue) nanoparticle catalysts are shown in Fig. 1(a). A straight line indicates that mass transfer limitations are negligible. The difference in slopes indicates different ΔE_{eff} values for the Pt and PtSn catalysts and different reaction mechanisms. The steeper slope observed with the Pt catalysts corresponds to an $\Delta E_{eff,Pt} = 133 \pm 25$ kJ/mol. This value is in general agreement with the $\Delta E_{eff,Pt}$ values previously reported for vapor-deposited Pt catalysts on SiO_2 supports (110 kJ/mol) [30], nanoparticle catalysts encapsulated in SiO_2 (115 kJ/mol),[18] and Pt single crystals (140 kJ/mol) [31]. In comparison, PtSn catalysts promote the CO oxidation reaction with an $\Delta E_{eff,PtSn} = 35.7 \pm 4$ kJ/mol. This value is consistent with $\Delta E_{eff,PtSn}$ observed from thermal induced desorption on a $Pt_3Sn(1\,1\,1)$-(2×2) single crystal (30.4 kJ/mol) [2] and ~3.8 nm Pt_3Sn nanoparticle catalysts supported on Al_2O_3 (31 kJ/mol) [32]. The difference in activation barriers is consistent with the increased activity observed previously with PtSn catalysts [1,2,6,33–36].

3.3. Kinetic reaction orders for O_2 for CO_2 production

The kinetic reaction orders for O_2 with respect to the rate of CO_2 formation were determined under low- and high-pressure conditions: at 200 °C with 100 mTorr CO and partial pressures of O_2 (P_{O2}) in the range of $20 \leqslant P_{O2} \leqslant 300$ mTorr and at 260 °C with 100 Torr CO and $40 \leqslant P_{O2} \leqslant 100$ Torr. The values of $n_{O2,PtSn}$ were determined from the slopes given by a $\ln(r)$–$\ln(P_{O2})$ relationship. The reaction order for O_2 under low- and high-pressure conditions on PtSn (blue) catalysts is shown in Fig. 1(b) and (c); a comparison with pure Pt nanoparticles (red) is given for the high-pressure conditions. The relative rates for each catalyst shown in the figures are dependent on the number of catalytic active sites. Since the number of active sites was not measured as discussed above, the rates should not be compared directly. The Pt catalysts exhibit a $n_{O2,Pt} = 1.06 \pm 0.18$, which is consistent with previous reports of CO oxidation on Pt surfaces [30,32,37–39]. A first-order dependence in O_2 is also consistent in low-pressure regimes [29,37] and corresponds with a reaction mechanism that is controlled by O_2 adsorption before dissociation or molecular O_2 adsorption. Dissociation is not the rate-limiting step on pure Pt surfaces because two sites are required and n_{O2} would be equal to 0.5.

On the PtSn nanoparticle catalysts, we observed a variation in $n_{O2,PtSn}$ with P_{O2}. When $P_{O2} < 90$ mTorr, $n_{O2,PtSn} = 0.47 \pm 0.02$, which is reflective of a reaction that is limited by molecular oxygen dissociation. However, when the ratio of O_2:CO increased to values above one, $n_{O2,PtSn}$ decreased to 0.27 ± 0.01. At high pressures with $P_{O2} > 40$ Torr with 100 Torr CO, $n_{O2,PtSn}$ exhibited a value of zero. We observed a discontinuous increase in the rate at $P_{O2} = 70$ Torr as the pressure was increased. This repeatable phenomenon may be related to a change in the surface structure of the catalyst; however, we did not pursue further investigations.

The transition from an effective half-order to zero-order reaction mechanism suggests dissociation is rate limiting at low pressures, and at higher pressures, the surfaces (and bulk) of Sn on the alloy nanoparticle catalyst are highly populated with atomic oxygen. This behavior can occur when the concentration of a given

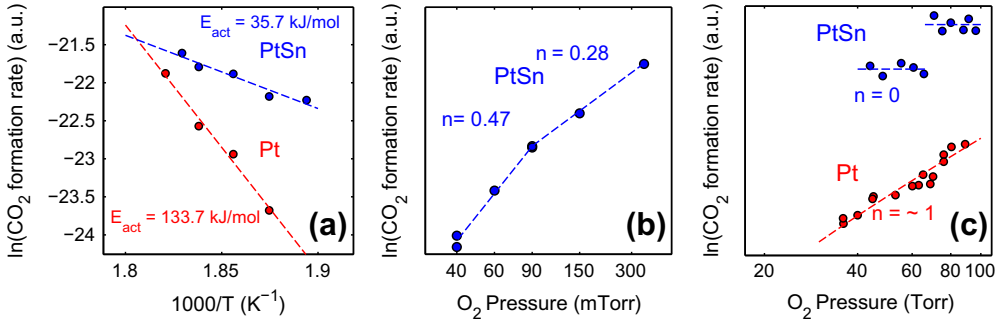

Fig. 1. (a) Arrhenius plot for CO_2 formation on 2 nm Pt (red) and 2 nm PtSn (blue) nanoparticle catalysts. The reaction rates were determined between 200 and 300 °C. (b) and (c) Plots of the ln(CO_2 formation rate) versus ln(P_{O2}) yield the reaction order in O_2 for 2 nm Pt (red) and 2 nm PtSn (blue) catalysts. (For interpretation of the references to color in this figure legend, the reader is referred to the web version of this article.)

species starts low and becomes sufficiently large that the species is not depleted as the reaction proceeds. Thus, in contrast to the pure Pt catalysts that are rate limited by O_2 adsorption when poisoned by CO, the trends observed on the PtSn catalyst are consistent with a reaction mechanism that is not inhibited by CO. In other words, Sn is a likely active center for O_2 adsorption and dissociation. A system consisting of Pt catalysts deposited onto a SnO_2 support was also found to have zero-order dependence in O_2 [40].

The kinetic reaction order for CO on Pt ($n_{CO,Pt}$) and PtSn ($n_{CO,PtSn}$) catalysts were also obtained (c.f. Fig. S2, Supporting information). Both catalysts exhibited nearly identical behaviors, which confirm that CO is interacting primarily with Pt active sites and Sn does not alter CO adsorption significantly.

3.4. Chemical states and composition of 2 nm PtSn nanoparticles under reaction conditions

To determine the chemical states and composition of the PtSn catalyst surface during reducing pre- and post-treatments and the active state of the catalyst surface during CO oxidation, we used *in situ* APXPS studies. The structure and surface composition of a catalyst often change when exposed to different gas atmospheres during pre- and post-treatments and reaction conditions [7–9,41,42]. A mutable catalyst surface can positively affect a reaction by providing a new and more facile reaction pathway or negatively affect a reaction by forming a core–shell structure that encapsulates one element in a binary nanoparticle. In some catalytic systems, surface structures that are formed after pre-treatment procedures degrade under reaction conditions only to leave an inactive catalytic surface [43]. In other cases, the phase of a catalyst that provides superior catalytic activity forms only under reaction conditions. In this work, we found that the surface of the PtSn catalyst changed with variations in the reaction atmosphere, which suggests a unique active phase that is formed only under reaction conditions. When exposed to a fully reducing atmosphere, XPS measurements indicate a surface consisting of a Pt–Sn intermixed phase. However, during reaction conditions, the surface was comprised of metallic Pt and Sn oxide domains. Given the surface-sensitivity of XPS, we infer that both Pt and Sn oxide reside on the surface.

The chemical states of Pt and Sn in the PtSn nanoparticle catalysts supported on a Si wafer were monitored during heat treatment in vacuum, pre-treatment reduction in H_2, CO and O_2 reaction mixtures, pure O_2 and post-treatment reduction in H_2. The chemical environment of the Sn in the PtSn nanoparticle catalysts was determined by monitoring photoemission of Sn $3d_{5/2}$ core-level electrons using a photon energy, $h\nu$ = 740 eV, which provides a kinetic energy for the photoelectrons of ~250 eV and an inelastic mean free path of 7 Å in a pure Sn environment [44]. The chemical environment of Pt was identified by monitoring photoemission of Pt 4f core-level electrons using $h\nu$ = 320 eV (to match the kinetic energy and probing depth used for the Sn). We also measured the chemical environment of O by monitoring photoemission of O 1s core-level electrons using $h\nu$ = 740 eV.

3.5. Reducing conditions

Following a heat treatment at 356 °C in vacuum and a reducing pre-treatment at 370 °C in 100 mTorr of H_2, the 2 nm PtSn nanoparticle surface was comprised of both Pt and Sn atoms. The Sn $3d_{5/2}$ (variations in blue) and Pt 4f doublet spectra (variations in green) measured during the reducing pre-treatment are shown in Fig. 2(a). The near surface composition of Pt and Sn in the PtSn nanoparticles determined from these spectra was 54% Pt and 46% Sn. These values are in agreement with the EDS results.

The Sn core-level spectrum under reducing pre-treatment conditions (Fig. 2(a)) exhibits three distinct chemical states. The spectrum is deconvoluted into features assigned to metallic Sn (Sn^0), Sn in a Pt environment ($Sn^{(Pt)}$), and a Sn^{4+} oxide state at 485.2, 485.8, and 487.3 eV, respectively. The peak locations and FWHM of all core-level features described herein are presented in Table 1. The two metallic features reside within the previously reported range of binding energies of 484.7–485.8 eV [1,4,45–48]. The positive core-level shift of the $Sn^{(Pt)}$ feature with respect to the location of Sn^0 is consistent with electron exchange between the Pt and Sn atoms in an alloy environment [1,5,46,49]. Regions of alloyed Sn with Pt and isolated domains of the elements are possible with colloidally synthesized binary metal nanoparticles, which grow inhomogeneously due to different redox potentials of the elements and the statistically random nature of atomic attachment to the metal seed during the growth stage [50]. The Sn^{4+} core-level shift exceeds previous reports for bulk SnO_2 by 0.6 eV [1,51]. The binding energy shift is likely a property of the nanoparticle's dimensions [24,52,53]. A Sn^{2+} state, which has a photoemission feature at 486.4 eV, is not present under these reducing conditions. However, prior to pre-treatment, the PtSn nanoparticles exhibited Sn^0, $Sn^{(Pt)}$, Sn^{4+}, and Sn^{2+} chemical states. XPS spectra of the Sn $3d_{5/2}$ core-level electrons over the course of an hour and temperatures of 200–370 °C in vacuum – prior to exposure to the H_2 atmosphere – and the progression of the Sn^0, $Sn^{(Pt)}$, Sn^{2+}, and Sn^{4+} states during the treatment are shown in Figs. S4 and S5 in the Supporting

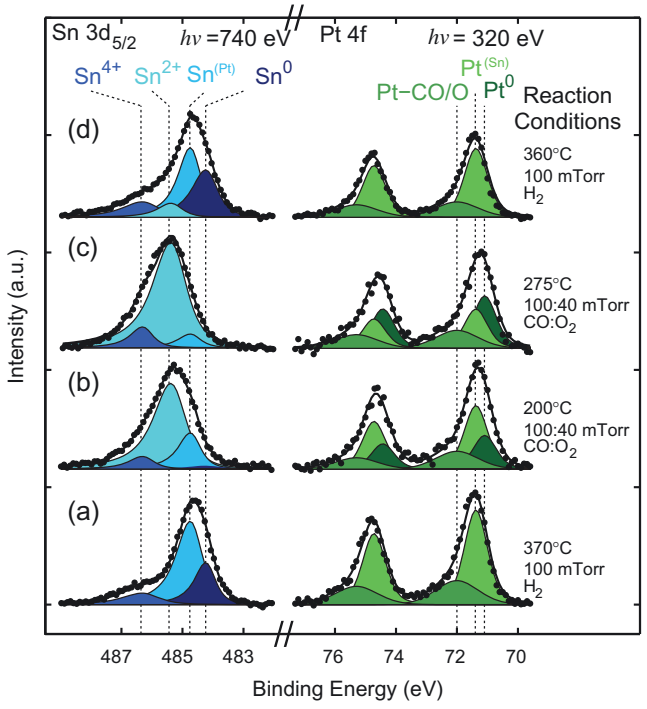

Fig. 2. *In situ* Sn $3d_{5/2}$ (variations in blue) and Pt 4f (variations in green) ambient pressure X-ray photoelectron spectra for 2 nm PtSn nanoparticle catalysts during (a) pre-treatment reduction in 100 mTorr H_2 at 370 °C, (b) reaction conditions with 100 mTorr CO and 40 mTorr O_2 at 200 °C, (c) reaction conditions with 100 mTorr CO and 40 mTorr O_2 at 275 °C, and (d) post-treatment in 100 mTorr H_2 at 360 °C. The Sn $3d_{5/2}$ spectra are deconvoluted into peaks assigned to metallic Sn (Sn^0), Sn in a Pt environment ($Sn^{(Pt)}$), Sn^{2+}, and a Sn^{4+} oxide state at 485.2, 485.8, 486.4 and 487.3 eV, respectively. The Pt 4f spectra are deconvoluted into peaks assigned to metallic Pt (Pt^0), Pt in a Sn environment ($Pt^{(Sn)}$), and a feature that possibly includes Pt bound to chemisorbed CO, O, and Pt-carbonyl from the capping agent (Pt–CO/O) at 70.8, 71.4, and 72.5 eV. The spectra indicate that PtSn catalysts segregate into Sn^{2+} and Pt^0 domains under reaction conditions from an intermixed Pt and Sn domain under H_2 reducing conditions. (For interpretation of the references to color in this figure legend, the reader is referred to the web version of this article.)

information, respectively. As the PtSn nanoparticles were heated in vacuum to 356 °C, the concentration of oxide features diminished at the benefit of the Sn^0 and $Sn^{(Pt)}$ components. While Sn^{4+} remained following treatment, the Sn^{2+} was completely reduced.

The Pt $4f_{7/2}$ orbital spectra are deconvoluted into two features for each hybrid state: Pt in a Sn environment ($Pt^{(Sn)}$) located at 71.4 eV, which complements the $Sn^{(Pt)}$ feature and a relatively broad feature at 72.5 eV that possibly includes Pt bound to chemisorbed CO, O, and Pt-carbonyl from the polyvinylpyrrolidone (PVP) capping agent (Pt–CO/O) [4,26]. A shift of the Pt core-level electrons in X-ray absorption studies (i.e., whiteline position) has also been observed in the presence of Sn for Pt_xSn alloy nanoparticle catalysts [54]. The combination feature at 72.5 eV does not include Pt oxides, which exhibit a $Pt_{7/2}$ core-level feature that appears above 73 eV [6,26,54,55]. Matching Pt $4f_{5/2}$ hybrid orbital features are shown with a spacing of 3.3 eV above the Pt $4f_{7/2}$ orbital.

The chemical states of O during reducing and reaction environments are shown by photoemission of O 1s core-level electrons in the XPS spectra in Fig. S6 of the Supporting information. The O 1s spectrum shows no indication of O in Sn oxide during reducing pre-treatments.

As a reference for the different chemical states of Pt, Sn, and O, we characterized nanoparticles of pure Pt, pure Sn, and PtSn *ex situ* under vacuum conditions using a lab-based XPS system. A comparison of the Pt 4f, Sn $3d_{5/2}$, and O 1s spectra for the three nanoparticle systems after a reduction treatment at 350 °C in 1 atm of H_2 and transfer through ambient conditions to the analysis chamber is shown in Fig. S2 of the Supporting information.

3.6. Reaction conditions

The active phase of the PtSn catalysts under a reaction atmosphere of 100 mTorr CO and 40 mTorr O_2 at 200 °C is shown in Fig. 2(b). The gas-phase ratio used in the APXPS studies matches the gas ratio used in the kinetic studies with excess CO to poison the Pt sites. An XPS signal corresponding to CO_2 in the O 1s XPS spectrum (shown in Fig. S6(c)) and measurements using a quadruple mass spectrometer operating inside the XPS (not shown) confirm that the PtSn catalyst produces rapid turnover to CO_2.

Two changes occurred in the Sn and Pt XPS spectra with respect to the chemical states during reducing atmospheres: (1) a Sn^{2+} feature located at 486.4 eV appeared at the expense of $Sn^{(Pt)}$ and Sn^0 and (2) a feature at 70.8 eV corresponding to Pt^0 that is not near Sn atoms increased at the expense of $Pt^{(Sn)}$ and Pt–CO/O. The Pt^0 feature is located 0.6 eV lower than the Pt(Sn) feature and is consistent with the binding energy of bulk metallic Pt [26]. Continuing with a gaseous atmosphere of 100 mTorr CO and 40 mTorr O_2 at a higher temperature of 275 °C, the proportion of Sn^{2+} and Pt^0 increased further. The formation of Sn^{2+} and Pt^0 at the expense of the $Sn^{(Pt)}$ and $Pt^{(Sn)}$ intermixed domain indicates atomic segregation in the CO:O_2 reaction environment to form an active phase composed of Sn oxide and metallic Pt islands rather than an active phase composed of the intermixed alloy. The XPS oxygen signal (O 1s spectrum shown in the Supporting information) also exhibits a feature that is consistent with oxidized Sn (Fig. S6).

3.7. Post-reaction reduction treatment

The formation of separate Pt^0 and Sn oxide domains determined by the unique XPS peaks was found to be reversible. The Sn $3d_{5/2}$ and Pt 4f spectra during post-treatment in 100 mTorr H_2 at 360 °C are shown in Fig. 2(d). Again, the dominant features in the Sn $3d_{5/2}$ spectra comprise Sn^0, $Sn^{(Pt)}$, and Sn^{4+}, while the dominant features in the Pt 4f spectra comprise $Pt^{(Sn)}$ and Pt–CO/O. Comparison of the Sn $3d_{5/2}$ and Pt 4f spectra during pre-treatment and post-treatment indicates that re-reducing the catalyst following the reaction prompted the Pt and Sn atoms to return to the physically-mixed, metallic state that was measured prior to performing the reaction. A minority amount of Sn^{2+} remained on the surface during the post-treatment reduction; however, the trends observed over the course of the post-treatment suggest that the Sn^{2+} will diminish completely. The XPS spectra over the course of the post-treatment and the progression of the Sn^0, $Sn^{(Pt)}$, Sn^{2+}, and Sn^{4+} states are shown in Figs. S7 and S8 of the Supporting information, respectively.

3.8. Progression of Sn and Pt chemical environment over the course of treatment

The progression of Sn^0, $Sn^{(Pt)}$, and Sn^{2+} and Pt^0 and $Pt^{(Sn)}$ from pre-treatment, reaction, and post-treatment conditions is shown in Fig. 3(a) and (b) for the Sn and Pt species, respectively. Neither Sn^{4+} nor Pt–CO/O compositions are shown in the figures because the chemical states exhibit negligible change when switching atmospheres. The two panels display a correlation between the $Sn^{(Pt)}$, Sn^0, and $Pt^{(Sn)}$ states and a correlation between the Sn^{2+} and Pt^0 states. Under reaction conditions, the concentration of the intermixed domains decreases while the metallic Pt and Sn oxide domains increase. Under reaction conditions at 275 °C, the concentration of Sn^{2+} reached ~82% with negligible Sn^0 while the $Sn^{(Pt)}$ state endured. The presence of the $Pt^{(Sn)}$ and $Sn^{(Pt)}$ states indicates that an interface remains between Pt and Sn rather than complete phase separation into separate particles. The increase in $Pt^{(Sn)}$ and reemergence of $Sn^{(Pt)}$ states during post-treatment also coheres with an interface where Sn^{2+} is reduced at the Pt interface and diffuses to form the intermixed Pt–Sn domains. Sn^0 that does not intermix with Pt is formed from the Sn^{2+} atoms that are located in the interior of the domains or in the subsurface/bulk of the nanoparticle.

Following the first pre-treatment, Sn^{4+} was observed with a composition of ~15% relative to all Sn species regardless of the gas atmosphere and temperature. The fact that Sn^{4+} does not increase in content (not shown) suggests that nanoparticles remain as in a single composite matrix rather than separate into isolated nanoparticles as was shown by Uemera et al. [54]. The presence of Sn^{4+} during the reaction conditions can be explained by a disproportionation mechanism of Sn^{2+}: $2\ Sn^{2+} \rightarrow Sn^0 + Sn^{4+}$. The disproportionation was shown previously by Axnanda et al. [1].

4. Discussion

The catalytic benefits of Sn when added to Pt catalysts for CO oxidation have been described by changes in the binding of CO and O to the catalyst surface. Both spectroscopic measurements and theoretical predications on $Pt_3Sn(1\,1\,1)$ alloy single crystal surfaces have indicated that Sn shifts the d-band of Pt away from the Fermi level, and thus reduces the adsorption strength of CO on Pt (i.e., electronic ligand effects) [5,49,56]. Reducing the binding strength of CO promotes desorption at lower temperatures and allows for O_2 adsorption; that is, the alloy reduces the effects of CO inhibition over the net oxidation rate. PtSn hollow adsorption sites on $Pt_3Sn(1\,1\,1)$ alloy single crystal surfaces were also proposed to be influential in the reaction. The hollow sites were proposed to have a lower activation barrier for O_2 adsorption and dissociation in the presence of CO (i.e., ensemble effects) [4]. Enhanced CO oxidation at the interface between Pt (with adsorbed CO) and Sn (with adsorbed O) has also been proposed using Pt supported on Sn oxide and inverse catalysts of Sn oxides supported on Pt single crystals [1,3,40,57,58]. Our results using real PtSn nanoparticle catalysts also indicate that a reaction at a metal/metal oxide interface is responsible for the high activity.

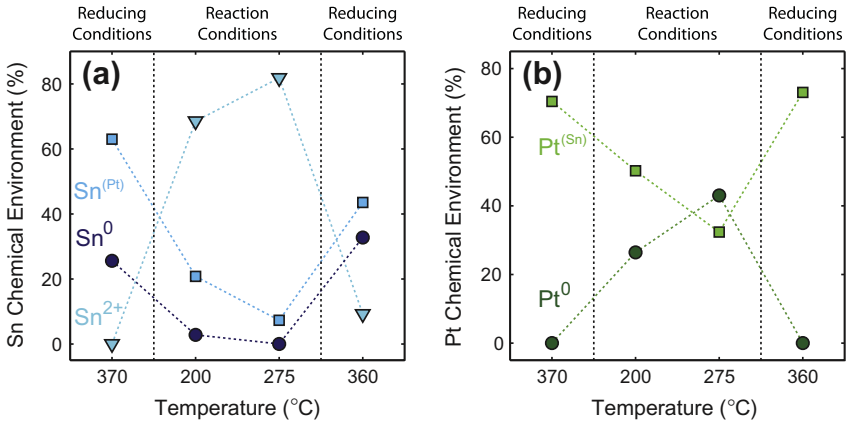

Fig. 3. Progression of the different chemical environments of (a) Sn and (b) Pt in the 2 nm PtSn nanoparticle catalysts when transitioning from pre-treatment, reaction, and post-treatment conditions. The trends for Sn^0, Sn(Pt), Sn^{2+}, Pt^0 and Pt(Sn) correspond to features in the ambient pressure X-ray photoelectron spectra in Fig. 2. Under H_2 reducing conditions, Sn^0, Sn(Pt), and Pt(Sn) are the dominant chemical states. During CO oxidation, the dominant chemical states are Sn^{2+} and Pt^0. The dynamic behavior suggests that the elements migrate to form distinguishable domains and the reaction occurs at a Pt/Sn oxide interface.

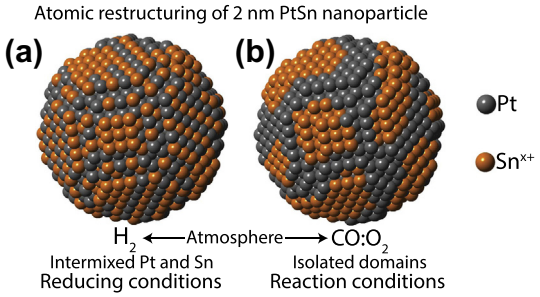

Fig. 4. Illustration of the segregation behavior between (a) intermixed Pt and Sn domains (reducing conditions) and (b) Pt and Sn oxide domains (reaction conditions) for a 2 nm PtSn nanoparticle. Pt and Sn atoms are gray and orange, respectively. The illustration does not distinguish between different chemical states of Pt and Sn. (For interpretation of the references to color in this figure legend, the reader is referred to the web version of this article.)

The spectroscopic results presented herein confirm that Pt and Sn are mobile within the nanoparticle and diffuse to form separate domains on the nanoparticle surface. The facile formation of isolated and intermixed domains suggests that Pt and Sn do not completely phase separate to form isolated nanoparticles. This behavior, which yields SnO_2, has been shown to occur under oxidizing conditions at temperatures above 350 °C [54]. As we determined when measuring the reference spectra, pure Sn is not readily reduced back to the lower oxidation states of Sn. Therefore, the reversible nature of Sn oxide to metallic Sn – and the formation of intermixed Pt and Sn domains – suggests that the atoms remain intact within a single nanoparticle composite. Under reducing conditions, the Pt and Sn atoms diffuse together to form a mixed phase, which was identified by the positive core-level shift in the XPS spectra. During CO oxidation, the spectroscopic signatures of intermixed Sn and Pt atoms disappeared at the expense of metallic Pt and oxidic Sn. In this picture, adsorbed CO resides on Pt domains, while O resides on or in the bulk of Sn domains. An illustration of the physical changes at the surface of 2 nm PtSn nanoparticle catalysts is shown in Fig. 4 with gray and orange atoms representing the Pt and Sn^{x+}, respectively, in (a) reducing and (b) reaction conditions. The illustration does not distinguish between different oxidation states of Sn.

The kinetic results corroborate the concept of different CO and O adsorption sites. In contrast to the first-order dependence observed for O_2 on the Pt catalysts, the dependence of O_2 for CO_2 formation on

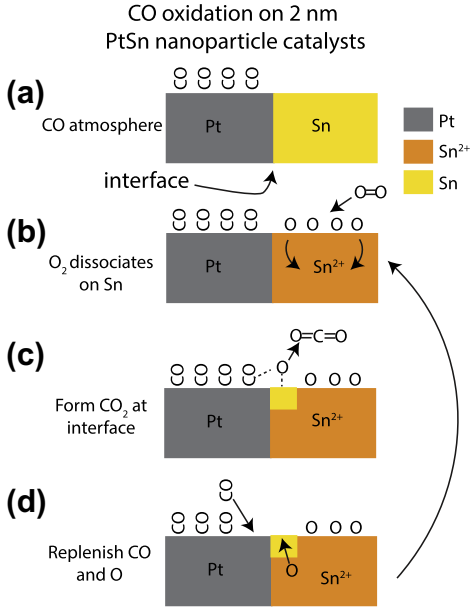

Fig. 5. Proposed mechanistic scheme for CO oxidation on 2 nm PtSn nanoparticles. Pt and Sn domains form an interface that exists at the nanoparticle surface under reaction conditions. CO is adsorbed only on Pt domains (a). When O_2 is added to the gas mixture, Sn^0/Sn(Pt) converts to Sn^{2+} (b). CO_2 is formed at the interface of Sn oxide and Pt domains whereby CO from Pt reduces a Sn^{2+}–Sn^0 redox couple (c) and the Sn site is replenished by O from the oxide reservoir (d).

the PtSn catalysts ranged from half- to zero-order with increased pressure. Pure Sn single crystals readily dissociate O_2 at room temperature to form chemisorbed surface Sn oxide with negligible activation barrier [59,60]. O also diffuses into the subsurface and bulk of Sn with low activation barriers (<30 kJ/mol) [46,59–61]. Thus, the trends from half- to zero-order dependence in O_2 for CO_2 formation on the PtSn nanoparticle catalyst can be related to dissociation of molecular oxygen at low partial pressures and surfaces that are highly concentrated with O adsorbed on/within the Sn domains of the nanoparticle at high pressures.

The active Sn oxide phase or the Sn species being reduced by CO remain under debate. Some reports argue that SnO_2 is the active state of the catalyst given the high concentration of the Sn^{4+} oxidation state observed during *ex situ* studies [3,34]. Others have argued that SnO is the active phase, including a recent study on a

$Pt_3Sn(1\,1\,1)$ single crystal that monitored the surface chemistry using APXPS [1,4]. The predominance of Sn^{2+} observed under reaction conditions in our study confirms that Sn^{2+} must be the active phase of Sn on PtSn nanoparticle catalysts, which agrees with the results from Axnanda et al. who showed this type of behavior with Sn nanoparticles deposited on Pt surfaces [1]. The likely mechanism for CO oxidation involves a redox shuttle at the interface of Pt and Sn with concerted renewal of O. There are two possible Sn redox couples: Sn^{4+}–Sn^{2+} or Sn^{2+}–Sn^0. Previous reports have shown that CO will not reduce SnO_2 [1,6,54,56,62] or a surface composed of 1 ML of SnO_2 deposited onto a $Pt(1\,1\,1)$ single crystal [1]. Moreover, we observed that SnO_2 will not completely reduce under a H_2 environment (H_2 has much higher reduction potential than CO). This indicates that a Sn^{4+}–Sn^{2+} redox couple is unlikely. Rather, CO reduces SnO located at the Pt/Sn interface with concerted renewal of O (Sn^{2+}–Sn^0 redox couple). This mechanism is depicted in Fig. 3, where a Pt–Sn interface is already formed. CO adsorbs only on the Pt domains and hinders O occupation; and thus, O adsorbs only on Sn domains. When the catalyst is exposed to CO and O_2 (Fig. 5(b)), O_2 dissociates on the surface of the Sn domains to form Sn^{2+} chemical states (e.g., SnO) [46]. Formation of subsurface and bulk Sn oxides has been shown previously on PtSn alloy and Sn single crystal surfaces [46,59,60]. CO_2 then forms from oxygen atoms at the edges of Sn domains (interface) by CO on the Pt domains.

5. Conclusions

PtSn catalysts provide an alternative and more facile reaction pathway for CO oxidation in comparison to pure Pt catalysts. We show that the kinetic mechanism of CO oxidation on PtSn catalysts is not limited by O_2 adsorption as observed on pure Pt catalysts. Instead, the PtSn catalyst is highly populated by O on the surface and subsurface regions of Sn. Ambient pressure X-ray photoelectron spectroscopy measurements of monodisperse PtSn nanoparticle catalysts showed that Pt and Sn atoms are mobile within the nanoparticles. The PtSn nanoparticles transform from intermixed Pt and Sn domains to metallic Pt and oxidic Sn domains during CO oxidation. While pure Pt catalysts displayed a reaction mechanism with an activation barrier of 133 kJ/mol, the PtSn catalysts displayed a reaction mechanism with an activation barrier of 35 kJ/mol. By intentionally poisoning the Pt sites with CO, we revealed that the low activation barrier was due to a redox reaction (Sn^{2+}–Sn^0 redox couple) that occurred at the interface of Pt and Sn oxide domains. We determined that the dominant chemical species of Sn was the partially oxidized Sn^{2+} rather than the fully oxidized Sn^{4+}. The high mobility of Pt and Sn in the nanoparticles and the reversibility of the chemical state with changing atmospheres make this catalytic system difficult to study using *ex situ* methods. The key to understanding the active phase of a catalyst is measuring the atomic-level properties under reaction conditions.

Acknowledgments

This research was funded by the U.S. Department of Energy, Office of Basic Energy Sciences, under contract no. DE-AC02-05CH11231. K.K. also acknowledges funding provided by the UCB–KAUST Academic Excellence Alliance (AEA) Program. This work was performed in part at the Molecular Foundry and the Advanced Light Source, beamline 9.3.2 of the Lawrence Berkeley National Laboratory. The Advanced Light Source is supported by the Director, Office of Science, Office of Basic Energy Sciences, of the U.S. Department of Energy under Contract No. DE-AC02-05CH11231.

Appendix A. Supplementary material

Supplementary data associated with this article can be found, in the online version, at http://dx.doi.org/10.1016/j.jcat.2014.01.005.

References

[1] S. Axnanda, W.P. Zhou, M.G. White, CO oxidation on nanostructured SnO_x/Pt(111) surfaces: unique properties of reduced SnO_x, Phys. Chem. Chem. Phys. 14 (2012) 10207–10214.
[2] C. Dupont, Y. Jugnet, F. Delbecq, D. Loffreda, Mediatory role of tin in the catalytic performance of tailored platinum-tin alloy surfaces for carbon monoxide oxidation, J. Catal. 273 (2010) 211–220.
[3] N.D. Gangal, N.M. Gupta, R.M. Iyer, Microcalorimetric study of the interaction of CO, O_2 and CO + O_2 with Pt/SnO_2 and SnO_2 catalysts, J. Catal. 126 (1990) 13–25.
[4] Y. Jugnet, D. Loffreda, C. Dupont, F. Delbecq, E. Ehret, F.J.C.S. Aires, B.S. Mun, F.A. Akgul, Z. Liu, Promoter effect of early stage grown surface oxides: a near-ambient-pressure XPS study of CO oxidation on PtSn bimetallics, J. Phys. Chem. Lett. 3 (2012) 3707–3714.
[5] P.N. Ross, Trends in the bonding of CO to the surfaces of Pt_3m alloys (M=Ti, Co, and Sn), J. Vac. Sci. Technol., A 10 (1992) 2546–2550.
[6] J. Singh, R.C. Nelson, B.C. Vicente, S.L. Scott, J.A. van Bokhoven, Electronic structure of alumina-supported monometallic Pt and bimetallic PtSn catalysts under hydrogen and carbon monoxide environment, Phys. Chem. Chem. Phys. 12 (2010) 5668–5677.
[7] J.R. Renzas, W.Y. Huang, Y.W. Zhang, M.E. Grass, D.T. Hoang, S. Alayoglu, D.R. Butcher, F. Tao, Z. Liu, G.A. Somorjai, $Rh_{1-x}Pd_x$ nanoparticle composition dependence in CO oxidation by oxygen: catalytic activity enhancement in bimetallic systems, Phys. Chem. Chem. Phys. 13 (2011) 2556–2562.
[8] F. Tao, M.E. Grass, Y.W. Zhang, D.R. Butcher, F. Aksoy, S. Aloni, V. Altoe, S. Alayoglu, J.R. Renzas, C.K. Tsung, Z.W. Zhu, Z. Liu, M. Salmeron, G.A. Somorjai, Evolution of structure and chemistry of bimetallic nanoparticle catalysts under reaction conditions, J. Am. Chem. Soc. 132 (2010) 8697–8703.
[9] F. Zheng, S. Alayoglu, V.V. Pushkarev, S.K. Beaumont, C. Specht, F. Aksoy, Z. Liu, J.H. Guo, G.A. Somorjai, In situ study of oxidation states and structure of 4 nm CoPt bimetallic nanoparticles during CO oxidation using X-ray spectroscopies in comparison with reaction turnover frequency, Catal. Today 182 (2012) 54–59.
[10] W.D. Michalak, J.M. Krier, K. Komvopoulos, G.A. Somorjai, Structure sensitivity in Pt nanoparticle catalysts for hydrogenation of 1,3-butadiene: in situ study of reaction intermediates using SFG vibrational spectroscopy, J. Phys. Chem. C 117 (2013) 1809–1817.
[11] S. Alayoglu, J. Krier, W.D. Michalak, Z. Zhu, E. Gross, G.A. Somorjai, In-situ surface and reaction probe studies with model nanoparticle catalysts, ACS Catal. 2 (2012) 2250–2258.
[12] Y.N. Xia, Y.J. Xiong, B. Lim, S.E. Skrabalak, Shape-controlled synthesis of metal nanocrystals: simple chemistry meets complex physics?, Angew Chem. Int. Ed. 48 (2009) 60–103.
[13] K. An, G.A. Somorjai, Size and shape control of metal nanoparticles for reaction selectivity in catalysis, Chemcatchem 4 (2012) 1512–1524.
[14] M. Salmeron, R. Schlogl, Ambient pressure photoelectron spectroscopy: a new tool for surface science and nanotechnology, Surf. Sci. Rep. 63 (2008) 169–199.
[15] D.E. Starr, Z. Liu, M. Havecker, A. Knop-Gericke, H. Bluhm, Investigation of solid/vapor interfaces using ambient pressure X-ray photoelectron spectroscopy, Chem. Soc. Rev. 42 (2013) 5833–5857.
[16] X.D. Wang, J. Stover, V. Zielasek, L. Altmann, K. Thiel, K. Al-Shamery, M. Baumer, H. Borchert, J. Parisi, J. Kolny-Olesiak, Colloidal synthesis and structural control of ptsn bimetallic nanoparticles, Langmuir 27 (2011) 11052–11061.
[17] Y.H. Jo, I. Jung, C.S. Choi, I. Kim, H.M. Lee, Synthesis and characterization of low temperature Sn nanoparticles for the fabrication of highly conductive ink, Nanotechnology 22 (2011).
[18] S.H. Joo, J.Y. Park, C.K. Tsung, Y. Yamada, P.D. Yang, G.A. Somorjai, Thermally stable Pt/mesoporous silica core-shell nanocatalysts for high-temperature reactions, Nat. Mater. 8 (2009) 126–131.
[19] W. Stober, A. Fink, E. Bohn, Controlled growth of monodisperse silica spheres in micron size range, J. Colloid Interface Sci. 26 (1968) 62–69.
[20] S. Ikeda, S. Ishino, T. Harada, N. Okamoto, T. Sakata, H. Mori, S. Kuwabata, T. Torimoto, M. Matsumura, Ligand-free platinum nanoparticles encapsulated in a hollow porous carbon shell as a highly active heterogeneous hydrogenation catalyst, Angew. Chem. Int. Ed. 45 (2006) 7063–7066.
[21] Z. Zhang, J.C. Li, Q. Jiang, Modelling for size-dependent and dimension-dependent melting of nanocrystals, J. Phys. D-Appl. Phys. 33 (2000) 2653–2656.
[22] Y.F. Zhu, J.S. Lian, Q. Jiang, Modeling of the melting point, Debye temperature, thermal expansion coefficient, and the specific heat of nanostructured materials (vol, 113C, pg 16898, J. Phys. Chem. C 113 (2009) (2009). 19748-19748.
[23] M.E. Grass, P.G. Karlsson, F. Aksoy, M. Lundqvist, B. Wannberg, B.S. Mun, Z. Hussain, Z. Liu, New ambient pressure photoemission endstation at Advanced Light Source beamline 9.3.2, Rev. Sci. Instrum. 81 (2010).
[24] H.G. Boyen, A. Ethirajan, G. Kastle, F. Weigl, P. Ziemann, G. Schmid, M.G. Garnier, M. Buttner, P. Oelhafen, Alloy formation of supported gold

nanoparticles at their transition from clusters to solids: Does size matter?, Phys Rev. Lett. 94 (2005).
[25] C.D. Wagner, L.E. Davis, M.V. Zeller, J.A. Taylor, R.H. Raymond, L.H. Gale, Empirical atomic sensitivity factors for quantitative-analysis by electron-spectroscopy for chemical-analysis, Surf. Interface Anal. 3 (1981) 211–225.
[26] D.R. Butcher, M.E. Grass, Z.H. Zeng, F. Aksoy, H. Bluhm, W.X. Li, B.S. Mun, G.A. Somorjai, Z. Liu, In situ oxidation study of Pt(110) and its interaction with CO, J. Am. Chem. Soc. 133 (2011) 20319–20325.
[27] A.K. Santra, D.W. Goodman, Catalytic oxidation of CO by platinum group metals: from ultrahigh vacuum to elevated pressures, Electrochim. Acta 47 (2002) 3595–3609.
[28] H. Steininger, S. Lehwald, H. Ibach, On the adsorption of Co on Pt(111), Surf. Sci. 123 (1982) 264–282.
[29] F. Gao, Y. Cai, K.K. Gath, Y. Wang, M.S. Chen, Q.L. Guo, D.W. Goodman, CO Oxidation on Pt-group metals from ultrahigh vacuum to near atmospheric pressures. 1. Rhodium, J. Phys. Chem. C 113 (2009) 182–192.
[30] S.M. McClure, M. Lundwall, Z. Zhou, F. Yang, D.W. Goodman, Characterization of Pt/SiO2 model catalysts at UHV and near atmospheric pressures, Catal. Lett. 133 (2009) 298–306.
[31] T.H. Lin, G.A. Somorjai, Modulated molecular-beam scattering of Co and No from Pt(111) and the stepped Pt(557) crystal-surfaces, Surf. Sci. 107 (1981) 573–585.
[32] M.M. Schubert, M.J. Kahlich, G. Feldmeyer, M. Huttner, S. Hackenberg, H.A. Gasteiger, R.J. Behm, Bimetallic PtSn catalyst for selective CO oxidation in H_2-rich gases at low temperatures, Phys. Chem. Chem. Phys. 3 (2001) 1123–1131.
[33] M. Boualleg, J.M. Basset, J.P. Candy, V. Caps, J.C. Jumas, S. Norsic, E.A. Quadrelli, L. Veyre, C. Thieuleux, Single-phase heterogeneous Pt_3Sn catalyst synthesized by room-temperature self-assembly, Chemcatchem 4 (2012) 1729–1732.
[34] J.L. Margitfalvi, I. Borbath, M. Hegedus, E. Tfirst, S. Gobolos, K. Lazar, Low-temperature CO oxidation over new types of Sn-Pt/SiO2 catalysts, J. Catal. 196 (2000) 200–204.
[35] E. Merlen, P. Beccat, J.C. Bertolini, P. Delichere, N. Zanier, B. Didillon, Characterization of bimetallic Pt-Sn/Al2O3 catalysts: relationship between particle size and structure, J. Catal. 159 (1996) 178–188.
[36] D.R. Schryer, B.T. Upchurch, B.D. Sidney, K.G. Brown, G.B. Hoflund, R.K. Herz, A Proposed Mechanism for Pt/SnO_x-Catalyzed CO Oxidation, J. Catal. 130 (1991) 314–317.
[37] A.D. Allian, K. Takanabe, K.L. Fujdala, X. Hao, T.J. Truex, J. Cai, C. Buda, M. Neurock, E. Iglesia, Chemisorption of CO and mechanism of CO oxidation on supported platinum nanoclusters, J. Am. Chem. Soc. 133 (2011) 4498–4517.
[38] P.J. Berlowitz, C.H.F. Peden, D.W. Goodman, Kinetics of Co oxidation on single-Crystal Pd, Pt, and Ir, J. Phys. Chem.-Us 92 (1988) 5213–5221.
[39] F. Gao, Y. Wang, Y. Cai, D.W. Goodman, CO Oxidation on Pt-group metals from ultrahigh vacuum to near atmospheric pressures. 2. Palladium and platinum, J. Phys. Chem. C 113 (2009) 174–181.
[40] K. Grass, H.G. Lintz, The kinetics of carbon monoxide oxidation on tin(IV) oxide supported platinum catalysts, J. Catal. 172 (1997) 446–452.
[41] J.Y. Park, Y. Zhang, S.H. Joo, Y. Jung, G.A. Somorjai, Size effect of RhPt bimetallic nanoparticles in catalytic activity of CO oxidation: Role of surface segregation, Catal. Today 181 (2012) 133–137.
[42] W.D. Michalak, G.A. Somorjai, Catalysis in energy: correlating composition, electronic structure and nanostructure with activity and selectivity using spectroscopy under working conditions (perspective), Top. Catal. 56 (2013) 1611–1622.
[43] A. Haghofer, D. Ferri, K. Föttinger, G. Rupprechter, Who is doing the job? Unraveling the role of Ga2O3 in methanol steam reforming on Pd2Ga/Ga2O3, ACS Catal. 2 (2012) 2305–2315.
[44] The inelasitc mean free path calculation was performed using the applet at http://www.lasurface.com/xps/imfpgrapher.php, which is based on the modeling functions from two publications: P.J. Cumpson and M.P. Seah, Elastic Scattering corrections in AES and XPS. II Estimating Attenuation Lengths and Conditions Required for their Valid Use in Overlayer/Substrate Experiments and M.P.Seah and W.A. Dench, Quantitative Electron Spectroscopy of Surfaces: A Standard Data Base for Electron Inelastic Mean Free Paths in Solids.
[45] A.H. Haner, P.N. Ross, U. Bardi, A. Atrei, Surface-composition determination of Pt-Sn alloys by chemical titration with carbon-monoxide, J. Vac. Sci. Technol., A 10 (1992) 2718–2722.
[46] D.I. Jerdev, B.E. Koel, Oxidation of ordered Pt-Sn surface alloys by O2, Surf. Sci. 492 (2001) 106–114.
[47] J.M. Themlin, M. Chtaib, L. Henrard, P. Lambin, J. Darville, J.M. Gilles, Characterization of tin oxides by X-Ray-photoemission spectroscopy, Phys. Rev. B 46 (1992) 2460–2466.
[48] P. Depadova, M. Fanfoni, R. Larciprete, M. Mangiantini, S. Priori, P. Perfetti, A synchrotron-radiation photoemission-study of the oxidation of tin, Surf. Sci. 313 (1994) 379–391.
[49] B. Hammer, Y. Morikawa, J.K. Norskov, CO chemisorption at metal surfaces and overlayers, Phys. Rev. Lett. 76 (1996) 2141–2144.
[50] R. Ferrando, J. Jellinek, R.L. Johnston, Nanoalloys: from theory to applications of alloy clusters and nanoparticles, Chem. Rev. 108 (2008) 845–910.
[51] J. Luo, C. Xu, XPS examination of tin oxide on float glass-surface, J. Non-Cryst. Solids 119 (1990) 37–40.
[52] W. Eberhardt, P. Fayet, D.M. Cox, Z. Fu, A. Kaldor, R. Sherwood, D. Sondericker, Photoemission from mass-selected monodispersed Pt clusters, Phys. Rev. Lett. 64 (1990) 780–784.
[53] N. Isomura, X.Y. Wu, H. Hirata, Y. Watanabe, Cluster size dependence of Pt core-level shifts for mass-selected Pt clusters on TiO2(110) surfaces, J. Vac. Sci. Technol., A 28 (2010) 1141–1144.
[54] Y. Uemura, Y. Inada, K.K. Bando, T. Sasaki, N. Kamiuchi, K. Eguchi, A. Yagishita, M. Nomura, M. Tada, Y. Iwasawa, Core-shell phase separation and structural transformation of $Pt3_Sn$ alloy nanoparticles supported on gamma-$Al2_O3$ in the reduction and oxidation processes characterized by in situ time-resolved XAFS, J. Phys. Chem. C 115 (2011) 5823–5833.
[55] L.K. Ono, B. Yuan, H. Heinrich, B.R. Cuenya, Formation and thermal stability of platinum oxides on size-selected platinum nanoparticles: support effects, J. Phys. Chem. C 114 (2010) 22119–22133.
[56] C. Xu, B.E. Koel, Probing the modifier precursor state – adsorption of CO on Sn/Pt(111) surface alloys, Surf. Sci. 304 (1994) L505–L511.
[57] R.K. Herz, A. Badlani, D.R. Schryer, B.T. Upchurch, Two-component catalysts for low-temperature CO oxidation: a Monte Carlo study, J. Catal. 141 (1993) 219–238.
[58] A. Boulahouache, G. Kons, H.G. Lintz, P. Schulz, Oxidation of carbon monoxide on platinum-tin dioxide catalysts at low temperatures, Appl. Catal. A 91 (1992) 115–123.
[59] J.F. Weaver, T.J. Campbell, G.B. Hoflund, G.N. Salaita, Oxidation of polycrystalline tin by hyperthermal atomic oxygen: an investigation using electron energy-loss spectroscopy, J. Electron. Spectrosc. 106 (2000) 81–91.
[60] G.B. Hoflund, G.R. Corallo, Electron-energy-loss study of the oxidation of polycrystalline tin, Phys. Rev. B 46 (1992) 7110–7120.
[61] N.A. Saliba, Y.L. Tsai, B.E. Koel, Oxidation of ordered Sn/Pt(111) surface alloys and thermal stability of the oxides formed, J. Phys. Chem. B 103 (1999) 1532–1541.
[62] Y. Uemura, Y. Inada, K.K. Bando, T. Sasaki, N. Kamiuchi, K. Eguchi, A. Yagishita, M. Nomura, M. Tada, Y. Iwasawa, In situ time-resolved XAFS study on the structural transformation and phase separation of Pt3Sn and PtSn alloy nanoparticles on carbon in the oxidation process, Phys. Chem. Chem. Phys. 13 (2011) 15833–15844.